

# Spectra and elliptic flow of light hadrons in an expanding fire-cylinder model for the RHIC Beam Energy Scan

Anand Rai<sup>✉,\*</sup>, Ashutosh Dwivedi<sup>✉,†</sup> and Sabyasachi Ghosh<sup>✉,‡</sup>

*Department of Physics, Indian Institute of Technology Bhilai, Kutalabhata, Durg, 491002, Chhattisgarh, India*

We investigate the transverse momentum spectra ( $p_T$ ) and elliptic flow ( $v_2$ ) of  $\pi^\pm$ ,  $K^\pm$ ,  $p$ , and  $\bar{p}$  produced in peripheral Au+Au collisions at  $\sqrt{s_{NN}} = 7.7, 11.5, 19.6, 27,$  and  $39$  GeV in the Beam Energy Scan (BES) Program at the Relativistic Heavy Ion Collider (RHIC). The analysis is carried out within an expanding elliptic fire-cylinder model that incorporates longitudinal expansion and anisotropic transverse flow. Particle production at kinetic freeze-out is obtained using a local equilibrium distribution function with a blast-wave-like fluid velocity profile derived from the expansion dynamics of the elliptic fire-cylinder. The model parameters governing the collective expansion are first constrained by fitting the midrapidity  $p_T$  spectra of  $\pi^\pm$  and are then applied, without further adjustment, to  $K^\pm$ ,  $p$ , and  $\bar{p}$ . The model provides a consistent description of the  $p_T$  spectra and reproduces the qualitative behavior of the elliptic flow for all considered particle species.

## I. INTRODUCTION

Relativistic heavy-ion collisions (HICs) provide a unique experimental environment to study strongly interacting matter at extreme temperatures and energy densities. Under such conditions, Quantum Chromodynamics (QCD) predicts a transition from confined hadronic matter to a deconfined quark-gluon plasma (QGP) [1–10]. Extensive experimental programs at the Relativistic Heavy Ion Collider (RHIC) [11, 12] and the Large Hadron Collider (LHC) [13, 14] have provided compelling evidence that the medium created in these collisions behaves as a strongly coupled, nearly perfect fluid. In particular, the observed small shear viscosity to entropy density ratio and the presence of pronounced collective flow are consistent with hydrodynamic evolution of a QGP formed in the hot and dense initial stage of the collision [15, 16]. Among the most informative observables are the transverse momentum ( $p_T$ ) spectra of identified hadrons and the anisotropic flow coefficients  $v_n$ , especially the elliptic flow [17, 18]. The  $p_T$  spectra carry information about the collective radial expansion and the kinetic freeze-out conditions of the system. The elliptic flow reflects the conversion of the initial spatial anisotropy of the collision zone into momentum-space anisotropy driven by pressure gradients [19–21]. The observed magnitude and mass ordering of  $v_2(p_T)$  provide strong evidence for early thermalization and the development of collective behavior in the medium [22, 23].

Relativistic hydrodynamics has been highly successful in describing collective phenomena such as particle spectra and flow over a wide range of collision energies and system sizes [19, 24–29]. Owing to the numerical complexity of full hydrodynamic simulations, simplified models inspired by hydrodynamics—commonly referred to as blast-wave (BW) models—are widely used

to describe particle spectra and collective flow [20, 30–47]. In these models, the medium expansion is characterized by a parametrized collective velocity field and a freeze-out hypersurface [48]. The commonly used BW parametrization assumes radially increasing transverse flow together with boost-invariant longitudinal expansion and freeze-out at fixed proper time, which provides a good description of transverse momentum spectra at mid-rapidity [31, 49]. However, this description becomes inadequate for low-energy and peripheral HICs, where collective flow develops predominantly along the reaction plane. To address this, azimuthal anisotropy in the transverse flow and spatial emission geometry has been incorporated into BW models, enabling successful descriptions of elliptic flow [20, 35, 36, 38, 39, 41, 42]. In addition, spherical or spheroidal geometries with instantaneous freeze-out in laboratory time [45, 46] and viscous extensions including non-equilibrium corrections to the distribution function [50–56] have been proposed to improve the description of experimental observables.

In this work, we propose an alternative blast-wave-like expanding fire-cylinder model to describe the transverse momentum spectra and elliptic flow of protons, pions, and kaons in Au+Au collisions at RHIC energies,  $\sqrt{s_{NN}} = 7.7\text{--}39$  GeV, for the centrality class 40–60 %. In off-central HICs, the initial transverse geometry of the medium is anisotropic and can be approximated by an ellipse in the transverse plane. The subsequent evolution of the system involves anisotropic transverse expansion together with longitudinal expansion. The transverse size of the medium is governed by the time evolution of the major axis  $a$  (along the  $y$  direction) and the minor axis  $b$  (along the  $x$  direction), while the longitudinal extent is characterized by  $z_B$ . To parametrize the transverse expansion, or equivalently the time dependence of  $a$  and  $b$ , we follow the geometric parametrization of the bulk medium developed in Refs. [57–67], originally applied to thermal electromagnetic emission and heavy-quark diffusion. This approach of parameterizing the bulk medium expansion has never been used systematically for fitting transverse momentum spectra and elliptic flow of  $\pi$ ,  $K$ ,

\* ranand@iitbhilai.ac.in

† ashutoshdwivedi92@gmail.com

‡ sabya@iitbhilai.ac.in

and  $p$  across different beam energies, which is attempted in the present article. Our fits involve eight free parameters: the chemical potential  $\mu$  and temperature  $T$  at kinetic freeze-out, five parameters ( $A$ ,  $B$ ,  $v_\infty$ ,  $\Delta v$ , and  $v_0$ ) that characterize the time evolution of the longitudinal and transverse dimensions of the elliptic fire-cylinder, and the freeze-out time  $t_f$ . The parameters  $A$  and  $v_\infty$  describe a uniform expansion of the elliptic cross section. For a realistic off-central collision, however, the pressure gradient along the reaction plane is larger than that in the perpendicular direction, leading to a faster expansion along the direction of the impact parameter; this anisotropy in the transverse expansion rate is quantified by the parameters  $B$  and  $\Delta v$ . The longitudinal expansion is modeled using a longitudinal expansion velocity  $v_0$ , incorporating an initial longitudinal size  $z_0$ , which can be sizable at low collision energies. The resulting fluid velocity profile is constructed from the transverse and longitudinal expansion rates of the evolving elliptic fire-cylinder. Using the obtained fluid velocity profile and the Cooper–Frye freeze-out prescription [68], we calculate the rapidity distributions, transverse momentum spectra, and elliptic flow of light hadrons, namely  $\pi^\pm$ ,  $K^\pm$ , and  $p(\bar{p})$ . The transverse momentum spectra and elliptic flow have been compared with the experimental results to obtain suitable values of the parameters describing the evolution of the elliptic fire-cylinder.

The paper is organized as follows. In Sec. II, we present the formalism of the expanding elliptic fire-cylinder model and the expressions for particle spectra and elliptic flow. Section III describes the fitting procedure and discusses the resulting transverse momentum spectra and elliptic flow. Finally, Sec. IV summarizes the main findings and outlines possible directions for future work.

## II. FORMALISM

The theoretical calculation of the important observables in HICs—the light hadron spectra and flow requires the description of the expanding medium formed in HIC experiments. In this section, we have described the expanding elliptic fire-cylinder model used to characterize the space-time evolution of the hot and dense matter formed in relativistic HICs. The key ingredients of the model, including parameterization of the fluid velocity and subsequent evaluation of the particle spectra and flow, are discussed.

### A. The expanding elliptic fire-cylinder

We will describe the space-time evolution of the expanding medium, which will be essentially an expanding fire-cylinder with an elliptic cross section. The total volume of the cylinder at time  $t$  is parametrized as [61, 65],

$$V(t) = 2\pi a(t)b(t)z_B(t), \quad (1)$$

where  $a(t)$ ,  $b(t)$ , and  $z_B(t)$  denote the time-dependent boundary for the transverse semi-axes along the  $y$ ,  $x$  and the longitudinal axis along the  $z$  directions, respectively. The transverse and longitudinal scale parameters evolve according to [65]

$$a(t) = a_0 + v_\infty \left[ t - \frac{1 - e^{-At}}{A} \right] - \Delta v \left[ t - \frac{1 - e^{-Bt}}{B} \right], \quad (2)$$

$$b(t) = b_0 + v_\infty \left[ t - \frac{1 - e^{-At}}{A} \right] + \Delta v \left[ t - \frac{1 - e^{-Bt}}{B} \right], \quad (3)$$

$$z_B(t) = z_0 + v_0 t, \quad (4)$$

where  $a_0$ ,  $b_0$ , and  $z_0$  fix the initial transverse and longitudinal geometry of the overlap region. The initial size in the longitudinal as well as transverse directions is determined from the collision specifications, i.e., the beam energy and centrality. For each colliding beam, the energy per nucleon is given by  $E_{\text{beam}} = \frac{\sqrt{s_{\text{NN}}}}{2}$  which determines the Lorentz factor  $\gamma = \frac{E_{\text{beam}}}{m_N}$ , where  $m_N$  is the nucleon mass. The initial longitudinal size of the fire-cylinder can now be obtained as  $z_0 = \frac{a_0}{\gamma}$ , where  $a_0 = \sqrt{R^2 - b_0^2}$  with  $R$  being the radius of the colliding nuclei and  $b_0$  being half of the impact parameter. Our choice of describing the Au+Au collisions with centrality class 40–60% translates to initial sizes  $b_0 = 3.5$  fm and  $a_0 = 6.06$  fm. The quantity  $v_\infty$  denotes the asymptotic transverse expansion velocity, while  $\Delta v$  quantifies the strength of the anisotropic flow component. The parameters  $A$  and  $B$  control the time scales for the buildup of isotropic and anisotropic collective flow, respectively.  $v_0$  is the effective longitudinal expansion velocity. The transverse expansion rates are given by

$$\dot{a} = \frac{da}{dt} = v_\infty(1 - e^{-At}) - \Delta v(1 - e^{-Bt}), \quad (5)$$

$$\dot{b} = \frac{db}{dt} = v_\infty(1 - e^{-At}) + \Delta v(1 - e^{-Bt}). \quad (6)$$

We will express the fluid four-velocity using the expansion rates given above. Before writing the fluid profile, we briefly describe the coordinate system we will use in this work. In the transverse plane, we use the confocal elliptic coordinate system in which we have  $x = \lambda \sinh \xi \cos \theta$  and  $y = \lambda \cosh \xi \sin \theta$ , where  $\xi \geq 0$  and  $0 \leq \theta \leq 2\pi$ . For a given  $\lambda$  (corresponding to the focal length), these define a confocal ellipse (for constant  $\xi$ ) and a hyperbola (for constant  $\theta$ ) having their major axis aligned with the  $y$  axis. The system size in the transverse plane at time  $t$  is given by,

$$\frac{x^2}{b^2(t)} + \frac{y^2}{a^2(t)} \leq 1. \quad (7)$$

At a fixed time  $t$  we set-up an elliptic coordinate system with  $\lambda(t) = \sqrt{a(t)^2 - b(t)^2}$  and  $0 \leq \xi \leq \xi_{\text{max}}(t)$ ,

where  $\xi_{\max}(t) = \sinh^{-1} \frac{\dot{b}(t)}{\lambda(t)}$ . The jacobian for the coordinate transformation  $(x, y) \rightarrow (\xi, \theta)$  is given by,  $J(\xi, \theta) = \lambda^2(t) [\cosh^2 \xi \cos^2 \theta + \sinh^2 \xi \sin^2 \theta]$ .

The fluid four-velocity field is written as [48],

$$u^\mu = \gamma_T \cosh \eta_L \left( 1, \frac{v_x}{\cosh \eta_L}, \frac{v_y}{\cosh \eta_L}, \tanh \eta_L \right), \quad (8)$$

where  $\eta_L$  denotes the longitudinal fluid rapidity and  $\gamma_T = \frac{1}{\sqrt{1-v_x^2-v_y^2}}$  is the Lorentz gamma factor associated with transverse velocity. The transverse and longitudinal velocity components at the boundary (surface) of the elliptic fire-cylinder are obtained as

$$v_x^B = \dot{b} \cos \theta, v_y^B = \dot{a} \sin \theta, v_z^B = v_0. \quad (9)$$

Assuming the velocity increases as we move towards the boundary, we take the following ansatz for the fluid profile [61, 65]

$$v_x = \frac{r}{r_B} \dot{b} \cos \theta, v_y = \frac{r}{r_B} \dot{a} \sin \theta, v_z = \frac{z}{z_B} v_0. \quad (10)$$

The radial lengths are defined as,  $r = \sqrt{x^2 + y^2} \leq r_B$  and  $r_B = \sqrt{x_B^2 + y_B^2}$  where the coordinates at the transverse boundary is  $x_B = \lambda(t) \sinh \xi_{\max}(t) \cos \theta$  and  $y_B = \lambda(t) \cosh \xi_{\max}(t) \sin \theta$ . The longitudinal velocity is written in the same spirit as that of transverse ones with the longitudinal boundary  $z_B(t) = z_0 + v_0 t$ . We notice that in the limit  $z_0 = 0$  we get back the Bjorken flow [49]  $v_z = \tanh \eta_L \rightarrow \frac{z}{t}$  for the region  $-z_B \leq z \leq z_B$ .

The invariant momentum distribution is obtained using the Cooper–Frye prescription [68],

$$E \frac{d^3 N}{d^3 \vec{p}} = \frac{g}{(2\pi)^3} \int_\sigma f(x, p) p^\mu d\sigma_\mu, \quad (11)$$

where  $f$  is the single particle distribution function,  $g$  is the associated spin degeneracy factor and  $\sigma$  denotes the freeze-out hyper surface. We choose a constant lab time freeze-out at time  $t = t_f$  which corresponds to  $d\sigma_\mu = (d^3 x, \mathbf{0})$ . Eq. (11) now reduces to

$$E \frac{d^3 N}{d^3 \vec{p}} = \frac{g}{(2\pi)^3} \int E f(x, p) dx dy dz. \quad (12)$$

For our purpose we use the local thermal distribution to be the Bose–Einstein or Fermi–Dirac form depend on the particle type  $f(x, p) = \left[ \exp\left(\frac{u_\mu p^\mu - \mu}{T}\right) \mp 1 \right]^{-1}$ , where  $p^\mu = (m_T \cosh y_p, p_T \cos \phi_p, p_T \sin \phi_p, m_T \sinh y_p)$  with  $p_T = \sqrt{p_x^2 + p_y^2}$ ,  $m_T^2 = p_T^2 + m^2$ ,  $y_p = \frac{1}{2} \ln \frac{E+p_z}{E-p_z}$  and  $\phi_p$  is the momentum space azimuthal angle. Transforming to elliptic coordinates  $(\xi, \theta)$  and using the identity  $\frac{d^3 \vec{p}}{E} = p_T dp_T dy_p d\phi_p$ , Eq. (12) becomes

$$\frac{1}{2\pi p_T} \frac{d^3 N}{dp_T dy_p d\phi_p} = \frac{g}{(2\pi)^4} \int f\left(\frac{u_\mu p^\mu - \mu}{T_{\text{kin}}}\right) \times m_T \cosh y_p |J(\xi, \theta)| d\xi d\theta dz, \quad (13)$$

where we have  $u^\mu p_\mu = \gamma_T (m_T \cosh(\eta_L - y_p) - \vec{v}_T \cdot \vec{p}_T)$  and  $T(t = t_f) = T_{\text{kin}}$ . If one approximates the distribution with the Boltzmann distribution, the above integral simplifies to

$$\begin{aligned} \frac{1}{2\pi p_T} \frac{d^3 N}{dp_T dy_p d\phi_p} &= \frac{g e^{\mu/T_{\text{kin}}}}{(2\pi)^4} \int_0^{\xi_f} d\xi \int_0^{2\pi} d\theta \lambda_f^2 (\cosh^2 \xi \cos^2 \theta + \sinh^2 \xi \sin^2 \theta) e^{(\gamma_T p_T \frac{r}{r_B} (\dot{b} \cos \theta \cos \phi_p + \dot{a} \sin \theta \sin \phi_p))} \\ &\times \int_{-z_f}^{z_f} m_T \cosh y_p e^{-\gamma_T m_T \cosh(\eta_L - y_p)} dz, \end{aligned} \quad (14)$$

where  $\lambda_f = \lambda(t_f)$  is the focal length of the boundary ellipse at freeze-out,  $\xi_f = \xi_{\max}(t_f)$  parameterize the locus of the elliptic boundary at freeze-out, the velocity at freeze-out hyper surface are given by  $v_x = \frac{r}{r_B} \dot{b}(t_f) \cos \theta$  and  $v_y = \frac{r}{r_B} \dot{a}(t_f) \sin \theta$  with  $\frac{r}{r_B} = \sqrt{\frac{\sinh^2 \xi \cos^2 \theta + \cosh^2 \xi \sin^2 \theta}{\sinh^2 \xi_f \cos^2 \theta + \cosh^2 \xi_f \sin^2 \theta}}$ .

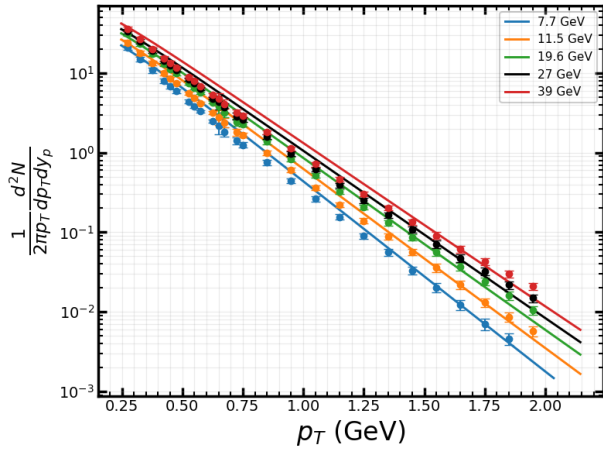
The elliptic flow coefficient is defined as [19]

$$v_2(y_p, p_T) = \frac{\int d\phi_p \cos(2\phi_p) \frac{d^3 N}{dp_T dy_p d\phi_p}}{\int d\phi_p \frac{d^3 N}{dp_T dy_p d\phi_p}}. \quad (15)$$

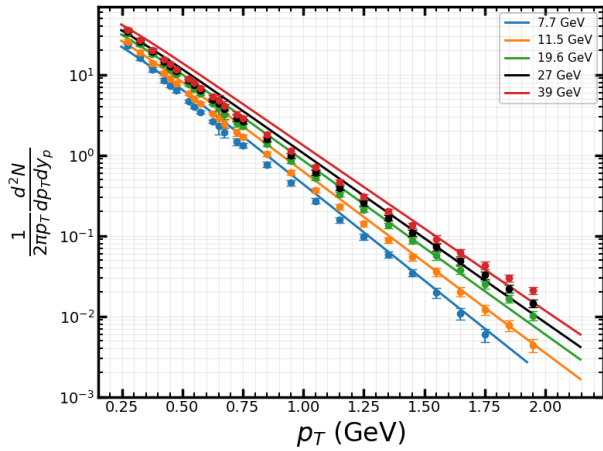
### III. RESULTS AND DISCUSSION

#### A. Momentum spectra

The model parameters governing the collective expansion, namely the asymptotic transverse velocity  $v_\infty$ , the anisotropic velocity component  $\Delta v$ , the longitudinal velocity  $v_0$ , and the flow buildup parameters  $A$  and  $B$ , are



(a)  $p_T$  spectra of  $\pi^+$  at mid-rapidity compared with STAR collaboration data [11].



(b)  $p_T$  spectra of  $\pi^-$  at mid-rapidity compared with STAR collaboration data [11].

FIG. 1: (Color online) Calculated  $p_T$  spectra of pions obtained using the fitted expansion parameters of Table I.

determined by fitting the transverse-momentum spectra of pions at mid-rapidity ( $y_p = 0$ ) for several values of the beam energy  $\sqrt{s_{NN}} = 7.7, 11.5, 19.6, 27, 39$  GeV. We take the pion chemical potential to be zero, i.e.,  $\mu_\pi = 0$ . The initial transverse dimensions  $a_0$  and  $b_0$  are kept fixed for all collision energies, reflecting the approximately energy-independent nuclear overlap geometry for a given centrality class, whereas  $z_0$  is taken as a function of  $\sqrt{s_{NN}}$  as discussed in Sec. II A. Fig. 1 illustrates this fit with the STAR collaboration data set [11]. Same set of collective expansion parameters and a single kinetic freeze-out temperature provide a good fit for both  $\pi^+$  and  $\pi^-$ , which justifies the assumption  $\mu_{\pi^+} = \mu_{\pi^-} = 0$ . Table I contains the model parameters calibrated with the help of experimental  $p_T$  spectra of the pion at mid-rapidity. One important parameter characterizing the geometry in the transverse plane is the spatial eccentricity. During system expansion, anisotropic pressure gradients drive a stronger expansion along the shorter axis ( $x$  axis),

leading to a continuous reduction of the spatial eccentricity with time [48]. We define the time-dependent spatial eccentricity as [69]

$$\epsilon(t) = \frac{a^2(t) - b^2(t)}{a^2(t) + b^2(t)}. \quad (16)$$

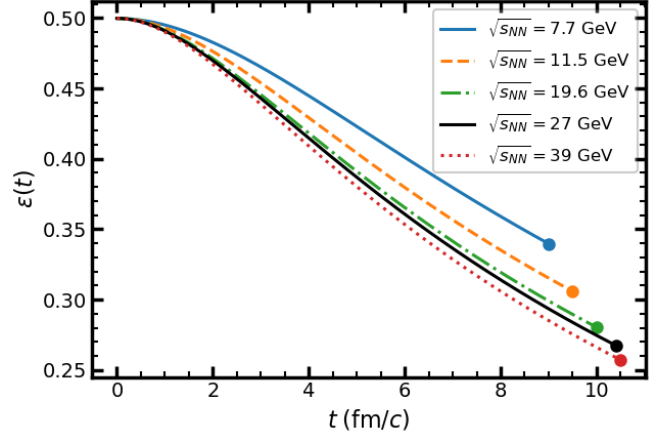


FIG. 2: (Color online) Time evolution of spatial eccentricity  $\epsilon(t)$  of the expanding elliptic fire-cylinder for different collision energies  $\sqrt{s_{NN}}$ . End points denote the freeze-out times for different  $\sqrt{s_{NN}}$ .

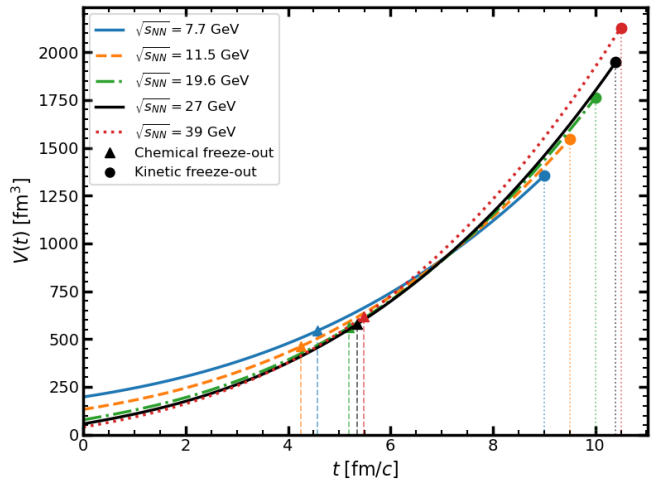


FIG. 3: (Color online) Time evolution of the volume  $V(t)$  of the expanding elliptic fire-cylinder for different collision energies  $\sqrt{s_{NN}}$ .

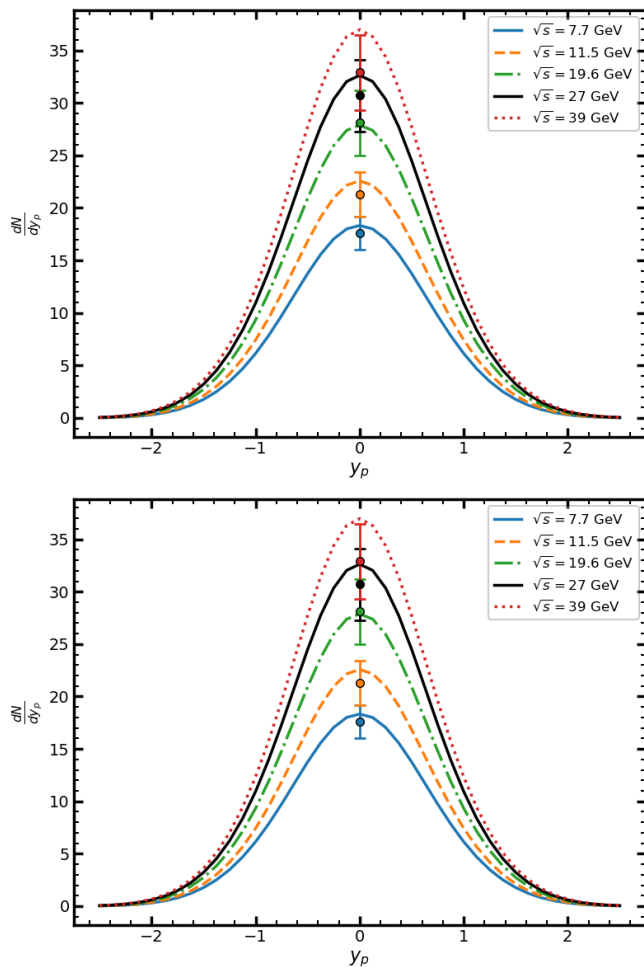


FIG. 4: (Color Online) Rapidity distribution of  $\pi^+$  (upper panel) and  $\pi^-$  (lower panel) for mid-central (40–50%) collisions at different beam energies  $\sqrt{s_{NN}}$  compared with the experimental data [11] at mid-rapidity.

Fig. 2 shows the time evolution of the spatial eccentricity for different beam energies  $\sqrt{s_{NN}}$  using the parameters obtained from fitting the pion spectra. At early times, the system exhibits a sizable eccentricity reflecting the initial geometric deformation. As the system evolves,

TABLE I: Fitted model parameters at different collision energies.

$\sqrt{s_{NN}}$ (GeV)	$T_{kin}$ (GeV)	$A$	$B$	$v_\infty$	$\Delta v$	$z_0$	$v_0$	$t_f$ (fm)
7.7	0.125	0.250	0.004	0.45	0.1	1.476	0.310	9.0
11.5	0.127	0.360	0.009	0.46	0.1	0.989	0.320	9.5
19.6	0.130	0.450	0.015	0.47	0.1	0.580	0.343	10.0
27	0.132	0.470	0.017	0.48	0.1	0.421	0.350	10.4
39	0.133	0.500	0.019	0.50	0.1	0.292	0.400	10.5

$\epsilon(t)$  decreases monotonically due to anisotropic collec-

tive expansion. The rate of this decrease is found to be stronger at higher collision energies, indicating more efficient pressure-driven expansion and a longer lifetime of the medium. Experimentally, the spatial eccentricity of the particle-emitting source at kinetic freeze-out can be extracted using azimuthally differential two-pion Hanbury Brown–Twiss (HBT) interferometry, through the oscillations of the HBT radii with respect to the reaction plane [36]. Using this method, the STAR Collaboration demonstrated that the freeze-out eccentricity remains finite but is significantly reduced compared to its initial value, and decreases systematically with increasing beam energy in Au+Au collisions [69]. Analysis in the same paper [69] also shows an increasing medium lifetime with the beam energy. The qualitative agreement between the present results and experimental observations [69] supports the consistency of our dynamical description of the fire-cylinder expansion. Similarly, using the chemical freeze-out analysis of the STAR collaboration, one can obtain the system volume at chemical freeze-out [11] (see appendix VID). These chemical freeze-out volumes, based on STAR collaboration data and kinetic freeze-out volumes, based on this fire-cylinder model, are denoted by triangle and circle points, respectively, in Fig. 3. Along with the graphical representation, those chemical and kinetic freeze-out volumes and times are tabulated in Table II. Observation of  $V_{ch}(t_{ch}) < V_{kin}(t_f)$  and  $t_{ch} < t_f$

TABLE II: Volume at kinetic and chemical freeze-out.

$\sqrt{s_{NN}}$ (GeV)	$t_{ch}$ fm	$V_{ch}$ fm <sup>3</sup>	$t_f$ fm	$V_{kin}$ fm <sup>3</sup>
7.7	4.56	541.74	9.0	1354.32
11.5	4.25	461.69	9.5	1546.56
19.6	5.18	559.25	10.0	1761.15
27	5.36	578.76	10.4	1947.43
39	5.48	620.01	10.5	2128.68

can be considered as a good consistency check of the hadronic phase evolution of the present model.

Another consistency check for the model is provided by obtaining the rapidity spectrum and comparing it with the experimental mid-rapidity yield [11]  $\left(\frac{dN}{dy_p}\right)_{y_p=0}$ . Rapidity distribution in low energy HICs remains Gaussian [45], we also observe a similar behavior in Fig. 4.

Once extracted as a result of fitting with the pion spectra, the resulting parameter sets  $(v_\infty, \Delta v, v_0, A, B, t_f, T_{kin})$  is applied consistently to the species  $K^\pm$  and  $p$  ( $\bar{p}$ ) without further modification of the collective dynamics. This strategy ensures a unified description of soft hadron production, where differences between particle species arise solely from their masses and chemical potentials. In Fig. 5, we show the  $p_T$  spectra of protons and kaons at mid-rapidity. In this procedure,  $\mu_p$  ( $\mu_{\bar{p}}$ ) and  $\mu_{K^+}$  ( $\mu_{K^-}$ ) is the only adjustable parameters for particle (anti-particle). The

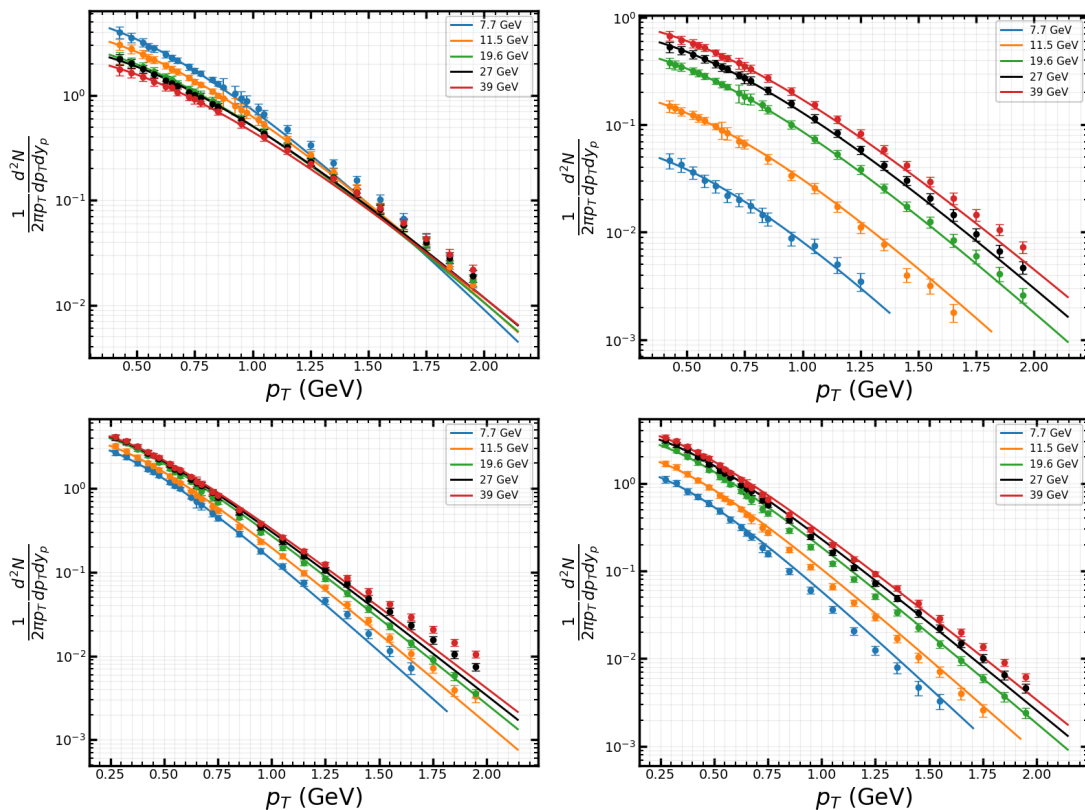


FIG. 5: (Color online) Calculated  $p_T$  spectra of protons ( $p$ ) (top-left), anti-protons ( $\bar{p}$ ) (top-right), positively charged kaons ( $K^+$ ) (bottom-left), and negatively charged kaons ( $K^-$ ) (bottom-right) at mid-rapidity compared with the data from [11].

resulting proton and anti-proton spectra are shown in the top-panel of Fig. 5. The model provides a simultaneous description of the spectral shape, indicating that the inclusion of a finite chemical potential is essential for reproducing proton (anti-proton) yields, particularly at lower beam energies where baryon stopping is significant [70, 71]. The extracted values of  $\mu_p$  (or  $\mu_{\bar{p}}$ ) can be seen in Table III. The transverse-momentum spectra of  $K^+$  and  $K^-$  are shown in bottom panel of Fig. 5. Our model also reproduces both the spectral shapes of  $K^+$  and  $K^-$  over the measured  $p_T$  range with chemical potential value of the kaons given in Table III. At this juncture we wish to mention that the measured value of the chemical potentials for the protons and the kaons at kinetic freeze-out are directly sensitive to the baryon ( $\mu_{\text{ch}}^B$ ) and strange ( $\mu_{\text{ch}}^S$ ) chemical potentials at chemical freeze-out for the Hadron-resonance gas system [11].

The beam-energy dependence of the rapidity distributions shows that the overall particle yield increases with increasing  $\sqrt{s_{\text{NN}}}$ , as expected from the larger initial entropy production at higher collision energies [8, 72]. We present the rapidity distribution of the  $p$  ( $\bar{p}$ ) and  $K^+$  ( $K^-$ ) in Fig. 6. The distribution appears Gaussian-like, similar to the pion rapidity distribution presented previously. In contrast to the high energy HICs where rapidity distributions show a plateau near mid-rapidity [73],

TABLE III: Chemical potentials  $\mu$  (GeV) for proton ( $p$ ), kaon $^+$  ( $K^+$ ), anti-proton ( $\bar{p}$ ), and kaon $^-$  ( $K^-$ ).

$\sqrt{s_{\text{NN}}}$	$\mu_p$	$\mu_{\bar{p}}$	$\mu_{K^+}$	$\mu_{K^-}$
7.7	0.323	-0.238	-0.040	0.151
11.5	0.263	-0.119	-0.045	0.124
19.6	0.197	-0.035	-0.046	0.096
27	0.167	-0.014	-0.061	0.097
39	0.124	-0.004	-0.080	0.106

low energy HICs show a Gaussian distribution [74, 75]. These Gaussian profiles have been observed in low energy HICs at CERN and GSI [74, 75]. We do not attempt a direct quantitative comparison with those results due to differences in the colliding system, collision energy, and centrality selection. However, we have shown the data of STAR collaboration [11] measured at mid-rapidity in Fig. 6, which are well fitted by the peak value of a Gaussian-like rapidity distribution, obtained from the present model.

By compiling Fig. 4 and 6, we can get the beam energy dependence of mid-rapidity particle yield  $dN/dy_p$  as a function of  $\sqrt{s_{\text{NN}}}$ , for  $\pi^+$ ,  $\pi^-$ ,  $K^+$ ,  $K^-$ ,  $p$ , and  $\bar{p}$ . The results are shown in Fig. 7 and Table IV, where

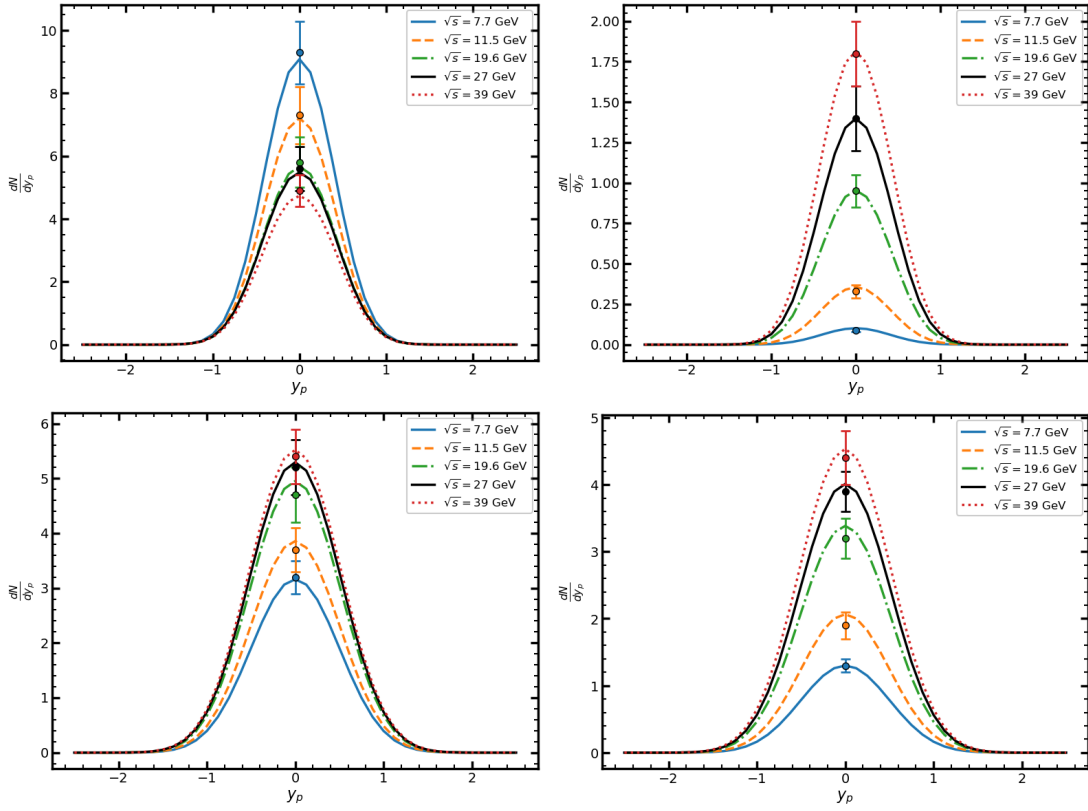


FIG. 6: Rapidity distribution of  $p$  (top-left),  $\bar{p}$  (top-right),  $K^+$  (bottom-left) and  $K^-$  (bottom-right) for mid-central (40–60%) collisions at different beam energies  $\sqrt{s_{NN}}$  compared with the data from [11].

experimental measurements are compared with the corresponding model calculations. The model calculations reproduce the overall energy dependence of the measured yields for all the particle species considered. In particular, the approximate equality of  $\pi^+$  and  $\pi^-$  yields indicates a negligible or minor charge chemical potential for the system. Quantitative differences between the model and experimental data remain within the experimental uncertainties, indicating that the essential features of particle production across the explored energy range are reasonably well described.

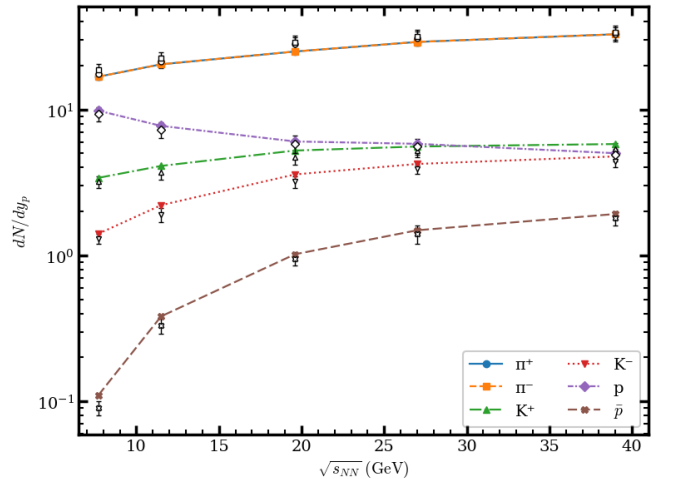


FIG. 7: Mid-rapidity particle yields  $dN/dy_p$  as a function of  $\sqrt{s_{NN}}$  for  $\pi^\pm$ ,  $K^\pm$ ,  $p$ , and  $\bar{p}$ . Symbols with error bars represent experimental data [11], while lines denote model calculations.

## B. Elliptic flow results

In addition to the transverse-momentum spectra, the present framework provides a simultaneous description

TABLE IV: Comparison of experimental and model-calculated midrapidity particle yields  $dN/dy_p$  for Au+Au collisions at different center-of-mass energies  $\sqrt{s_{NN}}$ . Experimental uncertainties are statistical only.

$\sqrt{s_{NN}}$ (GeV)	Particle	Exp.	model	Particle	Exp.	Model
7.7	$\pi^+$	$17.6 \pm 1.6$	16.79	$\pi^-$	$18.8 \pm 1.7$	16.79
	$K^+$	$3.2 \pm 0.3$	3.40	$K^-$	$1.3 \pm 0.1$	1.41
	$p$	$9.3 \pm 1.0$	9.82	$\bar{p}$	$0.09 \pm 0.01$	0.11
11.5	$\pi^+$	$21.3 \pm 2.1$	20.43	$\pi^-$	$22.5 \pm 2.3$	20.43
	$K^+$	$3.7 \pm 0.4$	4.10	$K^-$	$1.9 \pm 0.2$	2.21
	$p$	$7.3 \pm 0.9$	7.73	$\bar{p}$	$0.33 \pm 0.04$	0.38
19.6	$\pi^+$	$28.1 \pm 3.1$	24.99	$\pi^-$	$28.9 \pm 3.2$	24.99
	$K^+$	$4.7 \pm 0.5$	5.24	$K^-$	$3.2 \pm 0.3$	3.59
	$p$	$5.8 \pm 0.8$	6.04	$\bar{p}$	$0.95 \pm 0.10$	1.02
27	$\pi^+$	$30.7 \pm 3.4$	29.07	$\pi^-$	$31.5 \pm 3.5$	29.07
	$K^+$	$5.2 \pm 0.5$	5.58	$K^-$	$3.9 \pm 0.3$	4.24
	$p$	$5.6 \pm 0.7$	5.82	$\bar{p}$	$1.4 \pm 0.2$	1.49
39	$\pi^+$	$32.9 \pm 3.6$	32.81	$\pi^-$	$33.7 \pm 3.7$	32.81
	$K^+$	$5.4 \pm 0.5$	5.80	$K^-$	$4.4 \pm 0.4$	4.77
	$p$	$4.9 \pm 0.5$	5.02	$\bar{p}$	$1.8 \pm 0.2$	1.92

of the elliptic flow coefficient  $v_2$ . Using the same fire-cylinder geometry and hydrodynamic expansion parameters that were fixed from the fits to the identified-hadron  $p_T$  spectra, the calculated  $v_2(p_T)$  exhibits a qualitative agreement with the measured trends for pions, kaons, protons, and their corresponding anti-particles. In Fig. 8, we present the results of  $p_T$ -dependent elliptic flow at mid-rapidity along with the corresponding experimental data from STAR collaboration [76]. The predicted elliptic flow shows the characteristic rise with transverse momentum at low  $p_T$ , followed by a gradual saturation toward higher momenta. This behavior reflects the buildup of collective anisotropic flow driven by the initial spatial eccentricity and the subsequent pressure gradients, as originally proposed in Ref. [17] and extensively discussed in later theoretical and experimental studies [18, 24, 76]. Within the present model, the magnitude and shape of  $v_2(p_T)$  are governed by the transverse expansion parameter  $\Delta v$  and  $B$ , which control the strength and time development of the collective flow. In our calibration we fix  $\Delta v$  but increase  $B$  with increasing  $\sqrt{s_{NN}}$  (see Table I) which through Eqs. 5 and 6 imply a rapid development of anisotropic velocity part  $\Delta v$  in time (see Fig. 9). The increment in  $B$  makes the elliptic flow higher at higher  $\sqrt{s_{NN}}$ , which is reflected for all the considered particles in Fig. 8. We observe excellent quantitative agreement between our results and the experimental data for pions. For pions and kaons, the qualitative trend and ranking for different  $\sqrt{s}$  are not very different in our model calculation and experiments. However, for protons and anti-protons, an appreciable difference is observed. Since the number ( $\frac{dN}{dy_p}|_{y_p=0}$ ) of anti-protons is quite lower than that of protons and other mesons, its results may need a statistical fluctuation physics (event by event dynamics) consideration along with the thermalized statistical

physics. The negative value of the elliptic flow for anti-protons obtained in the experiments for  $\sqrt{s_{NN}}$  remains elusive. As discussed in Ref. [36], higher radial flow (corresponding to  $v_\infty$  in the present study) can make the  $v_2(p_T)$  for heavier particles negative at low  $p_T$ . Therefore, one may need to choose a larger radial boost for the anti-protons, as done in Ref. [39], to better align the results with the experimental data. However, we do not pursue it here in view of the simplicity of the model.

#### IV. SUMMARY

In summary, we study the transverse momentum spectra and elliptic flow of light hadrons produced in peripheral Au+Au collisions at the Relativistic Heavy Ion Collider for relatively low beam energies. The system formed in such collisions is modeled as an expanding cylinder with an elliptic cross section to account for the geometry of off-central collisions. The longitudinal and transverse expansion rates are parameterized using five unknown constants. The observables are calculated using the Cooper-Frye freeze-out prescription at a constant laboratory time, assuming a single-particle thermal equilibrium distribution function.

The midrapidity pion spectra are used to constrain the five expansion parameters, along with the kinetic freeze-out temperature and freeze-out time. The resulting parameters characterizing the transverse eccentricity and freeze-out time are found to be qualitatively consistent with results from identical-particle interferometry measurements, which probe the system at kinetic freeze-out. Assuming a single freeze-out hypersurface and using the parameters fixed from the pion spectra, we subsequently predict the spectra and elliptic flow of  $K^\pm$ ,  $p$ , and  $\bar{p}$ .

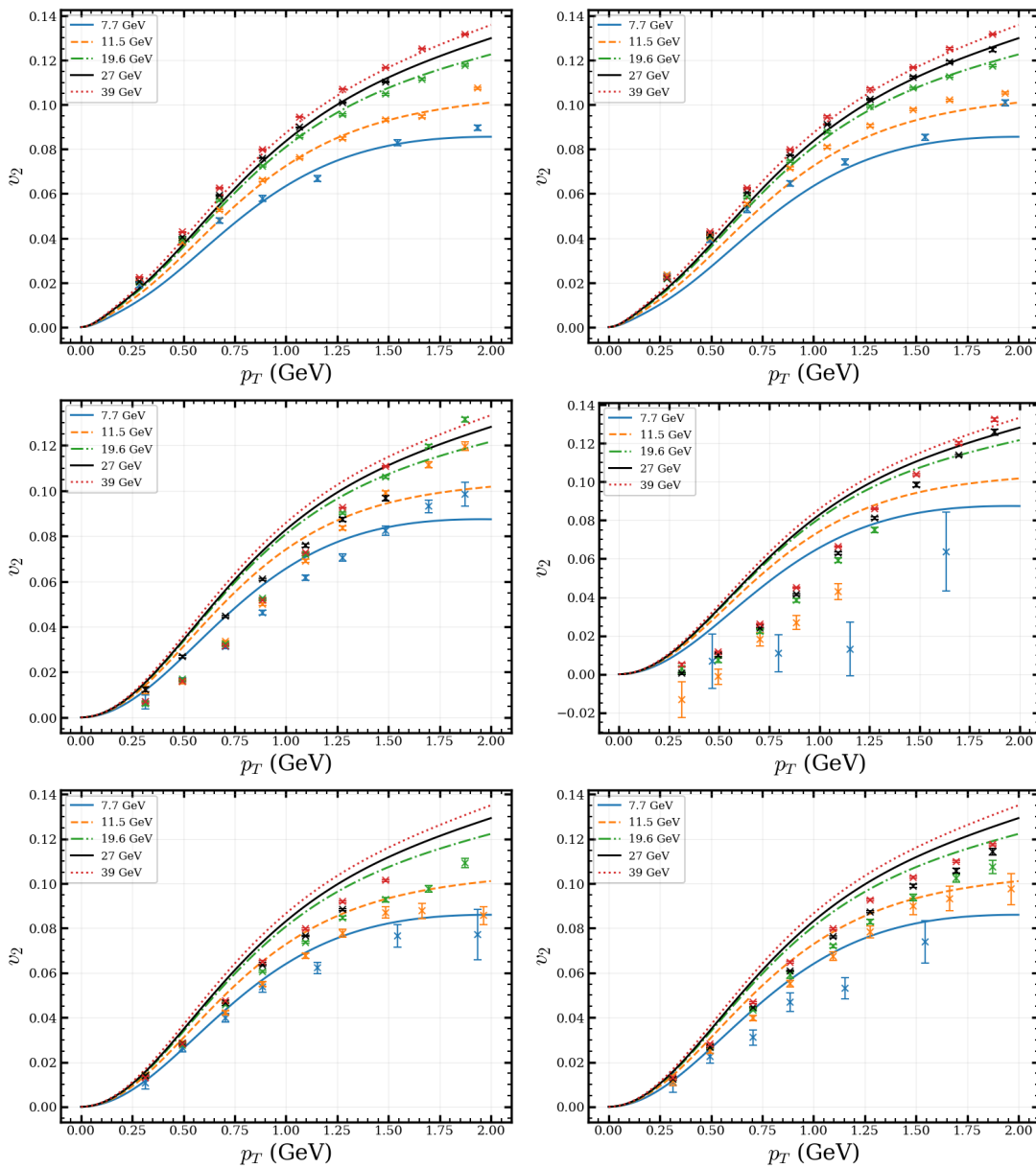


FIG. 8:  $p_T$  dependence of the elliptic flow  $v_2(p_T)$  for  $\pi^+$  (top-left),  $\pi^-$  (top-right),  $p$  (middle-left),  $\bar{p}$  (middle-right),  $K^+$  (bottom-left), and  $K^-$  (bottom-right) obtained using the same expansion parameters as in the  $\pi$  sector and chemical potentials from Table III is compared with the STAR data [76] of 0 – 80% centrality.

The predicted results are compared directly with experimental data to assess the quantitative agreement of the model. By introducing particle-specific chemical potentials for  $K^\pm$ ,  $p$ , and  $\bar{p}$  as additional fitting parameters, we are able to quantitatively reproduce their transverse momentum spectra. The elliptic flow of  $\pi^\pm$ ,  $K^\pm$ ,  $p$ , and  $\bar{p}$  obtained with the same set of model parameters shows overall qualitative agreement with experimental observations.

This work offers an alternative blast-wave-like parametrization for describing heavy-ion collisions at lower beam energies. For simplicity, several effects such

as resonance decays and baryon stopping, which may influence the observed spectra and flow, are not included in the present analysis and will be addressed in future studies. We plan to extend the model to additional beam energies and centrality classes, and to investigate higher-order flow observables such as triangular flow, as well as the effects of electromagnetic fields. Furthermore, once the soft-sector observables are well constrained, the model can be employed as a background framework to study penetrating probes such as heavy-quark diffusion and electromagnetic radiation.

## V. ACKNOWLEDGMENT

This work was supported in part by the Board of Research in Nuclear Sciences (BRNS) and the Depart-

ment of Atomic Energy (DAE), Government of India, with Grant Nos. 57/14/01/2024-BRNS/313 (A.R. and S.G.) and the Ministry of Education, Government of India (A.D.). The authors thank Sathwik HS, Ankit Kumar Panda, and Bhagyarathi Sahoo for fruitful discussions.

## VI. APPENDIX

### A. Shape and expansion of the transverse ellipse

In this appendix, we see the direction of the transverse velocity in relation to the periphery of the ellipse. Before that, it is worth mentioning that to obey the causality constraint we should have,

$$\begin{aligned} v_x^2 + v_y^2 &\leq 1 \\ \Rightarrow \dot{b}^2 \left( \frac{r \cos \theta}{r_B} \right)^2 + \dot{a}^2 \left( \frac{r \sin \theta}{r_B} \right)^2 &\leq 1. \end{aligned} \quad (17)$$

From which the sufficient condition becomes that the expansion velocity on the perimeter of the ellipse at the freeze-out time should be less than one, i.e.,  $\dot{b}^2(t_f) + \dot{a}^2(t_f) \leq 1$ .

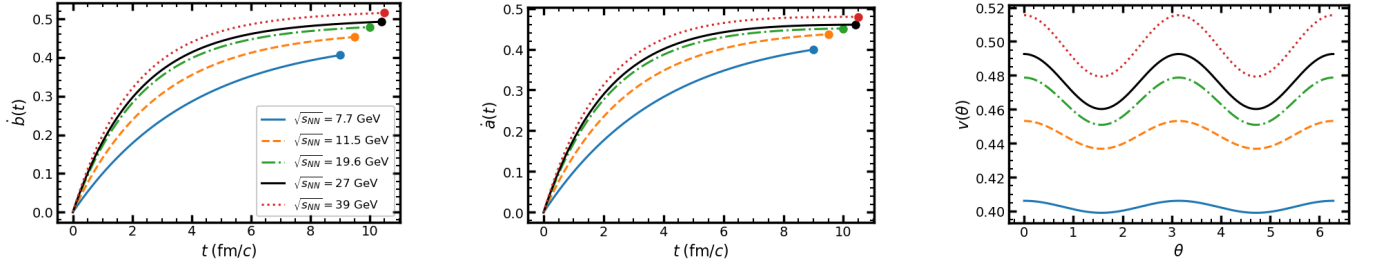


FIG. 9: Time evolution and angular dependence of the transverse expansion velocity of the fire-cylinder for different collision energies  $\sqrt{s_{NN}}$ .

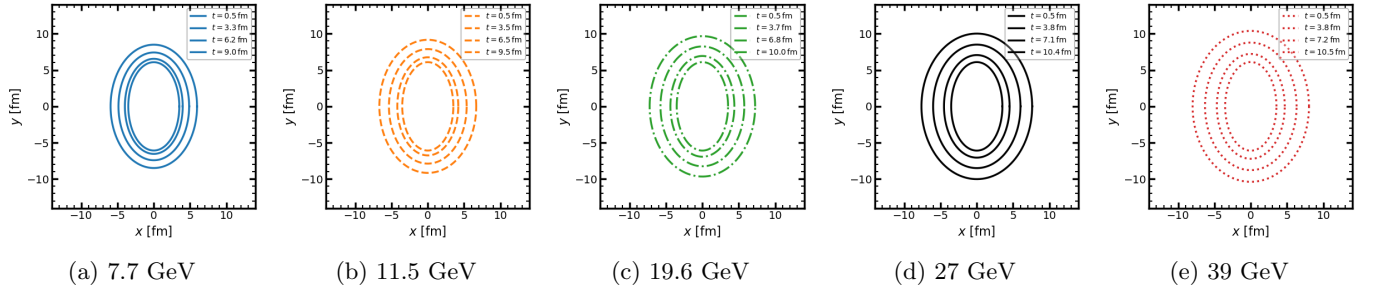


FIG. 10: Snapshots of the elliptical evolution of the expanding fire-cylinder at four different times.

To check the direction of the transverse velocity, we write down the tangent vector to the ellipse as,

$$\begin{aligned} \vec{n}_t(\xi, \theta) &= \frac{\partial \vec{r}_T}{\partial \theta} = \frac{\partial}{\partial \theta} (\lambda(t) \sinh \xi \cos \theta \hat{i} + \lambda(t) \cosh \xi \sin \theta \hat{j}) \\ &= -\lambda(t) \sinh \xi \sin \theta \hat{i} + \lambda(t) \cosh \xi \cos \theta \hat{j}. \end{aligned} \quad (18)$$

Taking the dot product of the transverse velocity  $\vec{v}_T$  with  $\vec{n}_t$  we have,

$$\begin{aligned} \vec{n}_t(\xi, \theta) \cdot \vec{v}_T &= (-\lambda(t) \sinh \xi \sin \theta \hat{i} + \lambda(t) \cosh \xi \cos \theta \hat{j}) \cdot \left( \frac{r}{r_B} \dot{b} \cos \theta \hat{i} + \frac{r}{r_B} \dot{a} \sin \theta \hat{j} \right) \\ &= -\lambda(t) \frac{r}{r_B} \sin \theta \cos \theta (\dot{b} \sinh \xi - \dot{a} \cosh \xi). \end{aligned} \quad (19)$$

From Eq. (19) we realize that for the velocity to be perpendicular to the elliptical boundary of the system we need  $\dot{a}(t)/\dot{b}(t) = \tanh \xi_{\max}(t)$  which in turn implies  $\lambda(t) = \text{constant}$ .

In Fig. 9, we display the expansion of the minor (along  $x$ ), major axis (along  $y$ ), and azimuthal variation of the velocity in the left, middle, and right panels, respectively. The expansion of the ellipse's axes is shown up to  $t = t_f(\sqrt{s_{\text{NN}}})$  for different beam energies. To display the azimuthal variation of the velocity, only the boundary ellipse at the freeze-out time  $t = t_f(\sqrt{s_{\text{NN}}})$  is considered. We observe that the rate of expansion increases with larger beam energies, as expected, because of the larger pressure gradients as the energy of the collisions increases. Similarly, one can observe a higher rate of expansion along the  $x$  axis than along the  $y$  axis, i.e.,  $\dot{b} > \dot{a}$ . The right panel of Fig. 9 essentially clarifies the beam energy dependence of  $v_2$  behavior observed in the Sec. III. A lesser azimuthal variation of the expansion velocity with decreasing  $\sqrt{s_{\text{NN}}}$  makes  $v_2$  smaller at lower  $\sqrt{s_{\text{NN}}}$ . Fig. 10 presents the snapshots of the medium in the transverse plane at different times. We can observe that the ellipses' eccentricities gradually decrease over time.

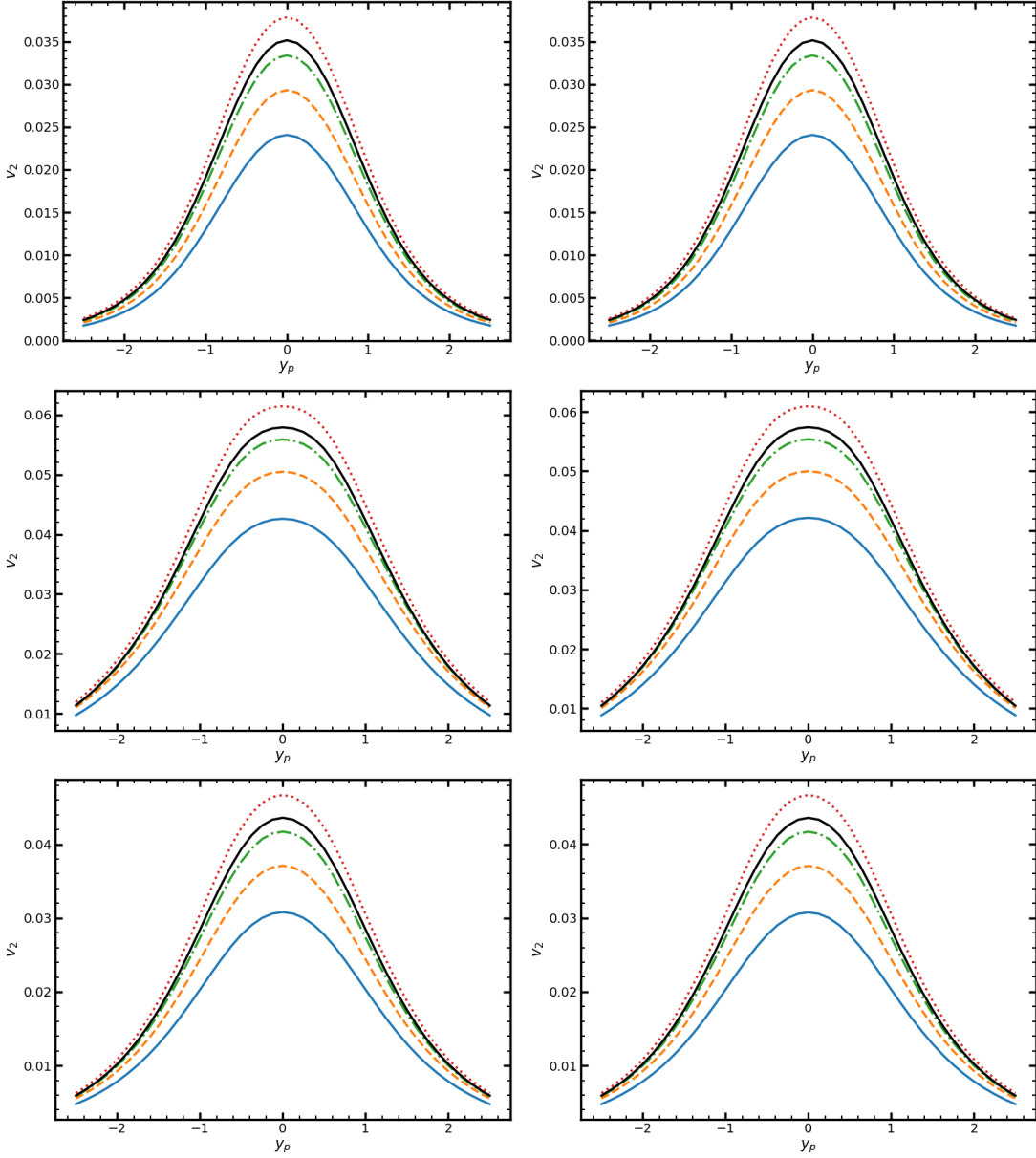


FIG. 11: Rapidity dependence ( $p_T$  integrated) of elliptic flow  $v_2$  for mid-central collisions at different beam energies  $\sqrt{s_{\text{NN}}}$  is shown for  $\pi^+$  (top-left),  $\pi^-$  (top-right),  $p$  (middle-left),  $\bar{p}$  (middle-right),  $K^+$  (bottom-left) and  $K^-$  (bottom-right).

## B. Rapidity dependence of elliptic flow

The dependence of the collective flow on rapidity provides important insights into the longitudinal dynamics of the expanding medium produced in relativistic HICs. In Fig. 11, we present the momentum-rapidity dependence of the elliptic flow coefficient  $v_2$  for mid-central collisions at different beam energies  $\sqrt{s_{\text{NN}}}$ . As shown in Fig. 11, the elliptic flow exhibits a pronounced maximum around mid-rapidity ( $y_p \approx 0$ ) and gradually decreases toward larger rapidities. This behavior reflects the reduced azimuthal anisotropy in the particle production as one moves away from the region of mid-rapidity.

## C. Statistical Analysis

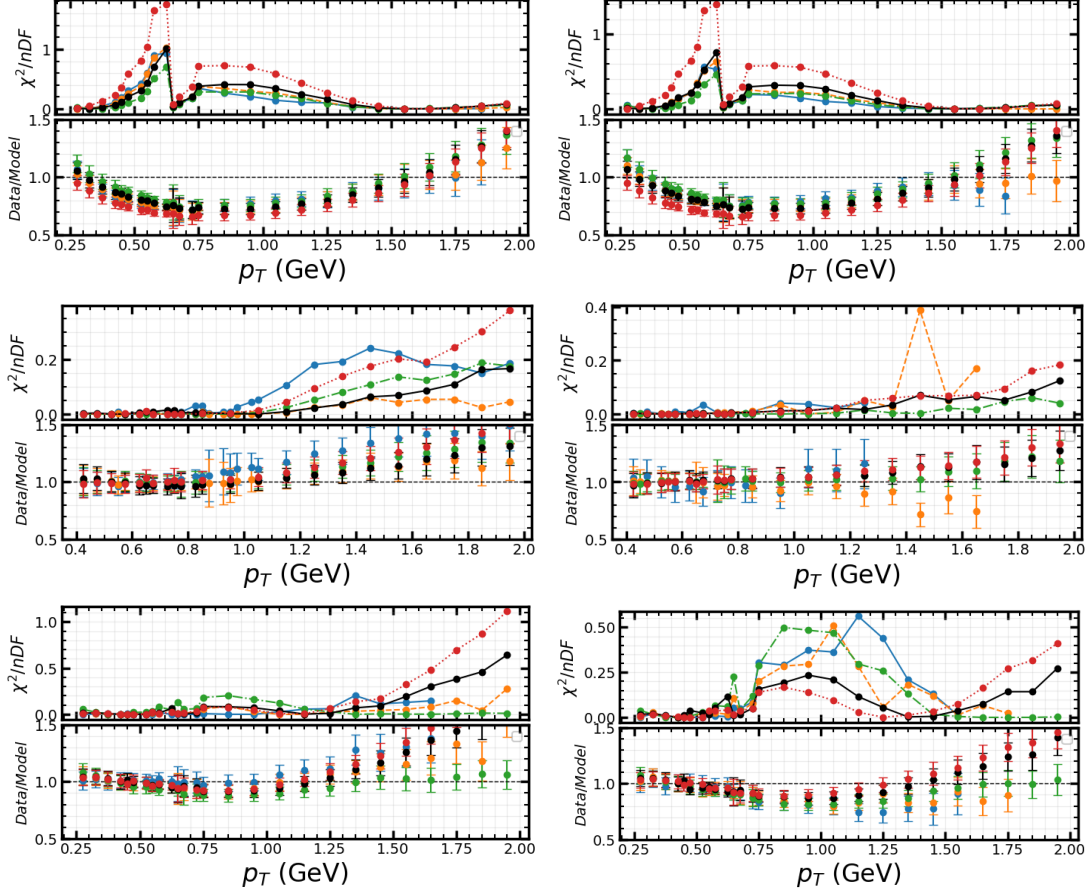


FIG. 12: (Color online) Deviations between the measured and fitted transverse momentum ( $p_T$ ) spectra for  $\pi^+$  (top left),  $\pi^-$  (top right),  $p$  (middle left),  $\bar{p}$  (middle right),  $K^+$  (bottom left), and  $K^-$  (bottom right).

The quality of the model description of the data was quantified using a  $\chi^2$  minimization procedure. The  $\chi^2$  function is defined as

$$\chi^2 = \sum_{i=1}^N \frac{(D_i - M_i)^2}{\sigma_i^2}, \quad (20)$$

where  $D_i$  denotes the experimental measurement,  $M_i$  the corresponding model prediction, and  $\sigma_i$  the total uncertainty of the data point. The larger uncertainty between the statistical ( $\sigma_{i,\text{stat}}$ ) and systematic ( $\sigma_{i,\text{syst}}$ ) uncertainties are used as  $\sigma_i$ . The number of degrees of freedom is defined as  $\text{nDF} = N - N_{\text{par}}$ , where  $N_{\text{par}}$  is the number of fit parameters. For the pion spectra we take  $N_{\text{par}} = 6$  ( $A, B, v_\infty, v_0, t_f, T$ ) and for proton and kaons we take  $N_{\text{par}} = 1$  (only chemical potential). The quantity  $\chi^2/\text{nDF}$  is displayed in the respective upper panels of the Fig.12. The quantity  $R_i = \frac{D_i}{M_i}$

(denoted as Data/Model) is also shown in the lower panels with uncertainties propagated from the experimental errors as  $\Delta R_i = \frac{\sigma_i}{M_i}$ .

#### D. Volume calculation from STAR Data [11]

The effective medium volume at chemical freeze-out is estimated from the measured particle multiplicity assuming thermal equilibrium and a Bose–Einstein (or Fermi–Dirac) distribution. To get the the particle yield we use

$$\begin{aligned}\Delta N &= \frac{dN}{dy_p} \Delta y_p, \\ &= n(\mu_{ch}, T_{ch}) \frac{dV}{dy_p} \Delta y_p, \\ &= n(\mu_{ch}, T_{ch}) V_{ch} \Delta y_p,\end{aligned}\tag{21}$$

where  $V_{ch} \equiv \frac{dV}{dy_p}$  is the effective volume per rapidity and  $n(\mu_{ch}, T_{ch})$  is the thermal number density. For a particle with mass  $m$ , the number density is given by

$$n(\mu_{ch}, T_{ch}) = \frac{1}{2\pi^2} \int_0^\infty \frac{p^2 dp}{\exp((E - \mu_{ch})/T_{ch}) \pm 1},\tag{22}$$

where the single-particle energy is  $E = \sqrt{p^2 + m^2}$  and the chemical potential  $\mu_{ch} = \mu_{ch}^B B_i + \mu_{ch}^Q Q_i + \mu_{ch}^S S_i$ . To estimate  $V_{ch}$ , we take the chemical freeze-out value of baryon, strange, and charge chemical potentials provided in the analysis of [11]. This results in different  $V_{ch}$  for different particles. The average volume  $V_{ch}$  of pion, proton, and kaon is shown in Fig. 3.

- 
- [1] Edward V. Shuryak. Quantum Chromodynamics and the Theory of Superdense Matter. *Phys. Rept.*, 61:71–158, 1980. doi:10.1016/0370-1573(80)90105-2.
- [2] Dirk H. Rischke. The Quark gluon plasma in equilibrium. *Prog. Part. Nucl. Phys.*, 52:197–296, 2004. arXiv:nucl-th/0305030, doi:10.1016/j.pnpnp.2003.09.002.
- [3] Edward V. Shuryak. What RHIC experiments and theory tell us about properties of quark-gluon plasma? *Nucl. Phys. A*, 750:64–83, 2005. arXiv:hep-ph/0405066, doi:10.1016/j.nuclphysa.2004.10.022.
- [4] Wit Busza, Krishna Rajagopal, and Wilke van der Schee. Heavy Ion Collisions: The Big Picture, and the Big Questions. *Ann. Rev. Nucl. Part. Sci.*, 68:339–376, 2018. arXiv:1802.04801, doi:10.1146/annurev-nucl-101917-020852.
- [5] John W. Harris and Berndt Muller. The Search for the quark - gluon plasma. *Ann. Rev. Nucl. Part. Sci.*, 46:71–107, 1996. arXiv:hep-ph/9602235, doi:10.1146/annurev.nucl.46.1.71.
- [6] John W. Harris and Berndt Müller. "QGP Signatures" Revisited. *Eur. Phys. J. C*, 84(3):247, 2024. arXiv:2308.05743, doi:10.1140/epjc/s10052-024-12533-y.
- [7] Peter Braun-Munzinger and Johanna Stachel. The quest for the quark–gluon plasma. *Nature*, 448(7151):302–309, 2007.
- [8] Anton Andronic, Peter Braun-Munzinger, Krzysztof Redlich, and Johanna Stachel. Decoding the phase structure of QCD via particle production at high energy. *Nature*, 561(7723):321–330, 2018. arXiv:1710.09425, doi:10.1038/s41586-018-0491-6.
- [9] Wojciech Florkowski. *Phenomenology of Ultra-Relativistic Heavy-Ion Collisions*. 3 2010.
- [10] Jean Letessier and Johann Rafelski. *Hadrons and Quark–Gluon Plasma*. Cambridge University Press, 11 2022. doi:10.1017/9781009290753.
- [11] L. Adamczyk et al. Bulk Properties of the Medium Produced in Relativistic Heavy-Ion Collisions from the Beam Energy Scan Program. *Phys. Rev. C*, 96(4):044904, 2017. arXiv:1701.07065, doi:10.1103/PhysRevC.96.044904.
- [12] Jinhui Chen et al. Properties of the QCD matter: review of selected results from the relativistic heavy ion collider beam energy scan (RHIC BES) program. *Nucl. Sci. Tech.*, 35(12):214, 2024. arXiv:2407.02935, doi:10.1007/s41365-024-01591-2.
- [13] G. Roland, K. Safarik, and P. Steinberg. Heavy-ion collisions at the LHC. *Prog. Part. Nucl. Phys.*, 77:70–127, 2014. doi:10.1016/j.pnpnp.2014.05.001.
- [14] Panagiota Foka and Małgorzata Anna Janik. An overview of experimental results from ultra-relativistic heavy-ion collisions at the CERN LHC: Bulk properties and dynamical evolution. *Rev. Phys.*, 1:154–171, 2016. arXiv:1702.07233, doi:10.1016/j.revip.2016.11.002.
- [15] Edward Shuryak. Why does the quark gluon plasma at RHIC behave as a nearly ideal fluid? *Prog. Part. Nucl. Phys.*, 53:273–303, 2004. arXiv:hep-ph/0312227, doi:10.1016/j.pnpnp.2004.02.025.
- [16] Paul Romatschke and Ulrike Romatschke. Viscosity Information from Relativistic Nuclear Collisions: How Perfect is the Fluid Observed at RHIC? *Phys. Rev. Lett.*, 99:172301, 2007. arXiv:0706.1522, doi:10.1103/

- PhysRevLett.* **99**.172301.
- [17] Jean-Yves Ollitrault. Anisotropy as a signature of transverse collective flow. *Phys. Rev. D*, 46:229–245, 1992. doi:10.1103/PhysRevD.46.229.
- [18] Sergei A. Voloshin, Arthur M. Poskanzer, and Raimond Snellings. Collective phenomena in non-central nuclear collisions. *Landolt-Bornstein*, 23:293–333, 2010. arXiv:0809.2949, doi:10.1007/978-3-642-01539-7\_10.
- [19] Peter F. Kolb and Ulrich W. Heinz. Hydrodynamic description of ultrarelativistic heavy ion collisions. pages 634–714, 5 2003. arXiv:nucl-th/0305084.
- [20] P. Huovinen, P. F. Kolb, Ulrich W. Heinz, P. V. Ruuskanen, and S. A. Voloshin. Radial and elliptic flow at RHIC: Further predictions. *Phys. Lett. B*, 503:58–64, 2001. arXiv:hep-ph/0101136, doi:10.1016/S0370-2693(01)00219-2.
- [21] Ekaterina Retinskaya, Matthew Luzum, and Jean-Yves Ollitrault. Constraining models of initial conditions with elliptic and triangular flow data. *Phys. Rev. C*, 89(1):014902, 2014. arXiv:1311.5339, doi:10.1103/PhysRevC.89.014902.
- [22] J. Adams et al. Azimuthal anisotropy in Au+Au collisions at  $\sqrt{s_{NN}} = 200$ -GeV. *Phys. Rev. C*, 72:014904, 2005. arXiv:nucl-ex/0409033, doi:10.1103/PhysRevC.72.014904.
- [23] B. I. Abelev et al. Mass, quark-number, and  $\sqrt{s_{NN}}$  dependence of the second and fourth flow harmonics in ultra-relativistic nucleus-nucleus collisions. *Phys. Rev. C*, 75:054906, 2007. arXiv:nucl-ex/0701010, doi:10.1103/PhysRevC.75.054906.
- [24] Ulrich Heinz and Raimond Snellings. Collective flow and viscosity in relativistic heavy-ion collisions. *Ann. Rev. Nucl. Part. Sci.*, 63:123–151, 2013. arXiv:1301.2826, doi:10.1146/annurev-nucl-102212-170540.
- [25] Charles Gale, Sangyong Jeon, and Bjoern Schenke. Hydrodynamic Modeling of Heavy-Ion Collisions. *Int. J. Mod. Phys. A*, 28:1340011, 2013. arXiv:1301.5893, doi:10.1142/S0217751X13400113.
- [26] Paul Romatschke and Ulrike Romatschke. *Relativistic Fluid Dynamics In and Out of Equilibrium*. Cambridge Monographs on Mathematical Physics. Cambridge University Press, 5 2019. arXiv:1712.05815, doi:10.1017/9781108651998.
- [27] A. De, J. I. Kapusta, M. Singh, and T. Welle. Comprehensive simulation of heavy-ion collisions at nonzero baryon chemical potential. *Phys. Rev. C*, 106(5):054906, 2022. arXiv:2206.02655, doi:10.1103/PhysRevC.106.054906.
- [28] Mahammad Sabir Ali, Deeptak Biswas, Amaresh Jaiswal, and Sushant K. Singh. Hadron momentum spectra from analytical solutions of relativistic hydrodynamics. *Eur. Phys. J. C*, 85(1):30, 2025. arXiv:2403.00624, doi:10.1140/epjc/s10052-025-13751-8.
- [29] Chiho Nonaka and Masayuki Asakawa. Modeling a realistic dynamical model for high energy heavy ion collisions. *Progress of Theoretical and Experimental Physics*, 2012(1):01A208, 09 2012. arXiv:https://academic.oup.com/ptep/article-pdf/2012/1/01A208/4456796/pts014.pdf, doi:10.1093/ptep/pts014.
- [30] Philip J. Siemens and John O. Rasmussen. Evidence for a blast wave from compressed nuclear matter. *Phys. Rev. Lett.*, 42:880–883, Apr 1979. URL: https://link.aps.org/doi/10.1103/PhysRevLett.42.880, doi:10.1103/PhysRevLett.42.880.
- [31] Ekkard Schnedermann, Josef Sollfrank, and Ulrich W. Heinz. Thermal phenomenology of hadrons from 200-A/GeV S+S collisions. *Phys. Rev. C*, 48:2462–2475, 1993. arXiv:nucl-th/9307020, doi:10.1103/PhysRevC.48.2462.
- [32] Wojciech Broniowski and Wojciech Florkowski. Explanation of the RHIC p(T) spectra in a thermal model with expansion. *Phys. Rev. Lett.*, 87:272302, 2001. arXiv:nucl-th/0106050, doi:10.1103/PhysRevLett.87.272302.
- [33] Wojciech Broniowski and Wojciech Florkowski. Strange particle production at RHIC in a single freezeout model. *Phys. Rev. C*, 65:064905, 2002. arXiv:nucl-th/0112043, doi:10.1103/PhysRevC.65.064905.
- [34] Wojciech Florkowski and Wojciech Broniowski. Hydro-inspired parameterizations of freeze-out in relativistic heavy-ion collisions. *Acta Phys. Polon. B*, 35:2895–2910, 2004. arXiv:nucl-th/0410081.
- [35] C. Adler et al. Identified particle elliptic flow in Au + Au collisions at  $\sqrt{s_{NN}} = 130$ -GeV. *Phys. Rev. Lett.*, 87:182301, 2001. arXiv:nucl-ex/0107003, doi:10.1103/PhysRevLett.87.182301.
- [36] Fabrice Retiere and Michael Annan Lisa. Observable implications of geometrical and dynamical aspects of freeze out in heavy ion collisions. *Phys. Rev. C*, 70:044907, 2004. arXiv:nucl-th/0312024, doi:10.1103/PhysRevC.70.044907.
- [37] Zebo Tang, Yichun Xu, Lijuan Ruan, Gene van Buren, Fuqiang Wang, and Zhangbu Xu. Spectra and radial flow at RHIC with Tsallis statistics in a Blast-Wave description. *Phys. Rev. C*, 79:051901, 2009. arXiv:0812.1609, doi:10.1103/PhysRevC.79.051901.
- [38] Min He, Rainer J. Fries, and Ralf Rapp. Scaling of Elliptic Flow, Recombination and Sequential Freeze-Out of Hadrons in Heavy-Ion Collisions. *Phys. Rev. C*, 82:034907, 2010. arXiv:1006.1111, doi:10.1103/PhysRevC.82.034907.
- [39] X. Sun, H. Masui, A. M. Poskanzer, and A. Schmah. Blast Wave Fits to Elliptic Flow Data at  $\sqrt{s_{NN}} = 7.7$ –2760 GeV. *Phys. Rev. C*, 91(2):024903, 2015. arXiv:1410.1947, doi:10.1103/PhysRevC.91.024903.
- [40] Ivan Melo and Boris Tomasik. Reconstructing the final state of Pb+Pb collisions at  $\sqrt{s_{NN}} = 2.76$  TeV. *J. Phys. G*, 43(1):015102, 2016. arXiv:1502.01247, doi:10.1088/0954-3899/43/1/015102.
- [41] Boris Tomasik. On elliptic flow and the blast-wave model. *Int. J. Mod. Phys. A*, 40(21):2542006, 2025. arXiv:2409.19758, doi:10.1142/S0217751X25420060.
- [42] Jakub Cimerman, Boris Tomasik, Mate Csanad, and Sandor Lokos. Higher-order anisotropies in the Blast-Wave Model - disentangling flow and density field anisotropies. *Eur. Phys. J. A*, 53(8):161, 2017. arXiv:1702.01735, doi:10.1140/epja/i2017-12349-7.
- [43] Ivan Melo and Boris Tomášik. Kinetic freeze-out in central heavy-ion collisions between 7.7 and 2760 GeV per nucleon pair. *J. Phys. G*, 47(4):045107, 2020. arXiv:1908.03023, doi:10.1088/1361-6471/ab5f03.
- [44] Wojciech Florkowski and Radoslaw Ryblewski. Statistical hadronization model for low-energy heavy-ion collisions. *Journal of Subatomic Particles and Cosmology*, 4:100249, 2025. URL: https://www.sciencedirect.com/science/article/pii/S3050480525002298, doi:10.1016/j.jspc.2025.100249.

- [45] Szymon Harabas, Wojciech Florkowski, Tetyana Galatyuk, Ź. Ma Lgorzata Gumberidze, Radosław Ryblewski, Piotr Salabura, and Joachim Stroth. Statistical hadronization model for heavy-ion collisions in the few-GeV energy regime. *Phys. Rev. C*, 102(5):054903, 2020. [arXiv:2003.12992](#), [doi:10.1103/PhysRevC.102.054903](#).
- [46] Szymon Harabas, Jędrzej Kolaś, Radosław Ryblewski, Wojciech Florkowski, Tetyana Galatyuk, Małgorzata Gumberidze, Piotr Salabura, Joachim Stroth, and Hanna Paulina Zbroszczyk. Spheroidal expansion and freeze-out geometry of heavy-ion collisions in the few-GeV energy regime. *Phys. Rev. C*, 107(3):034917, 2023. [arXiv:2210.07694](#), [doi:10.1103/PhysRevC.107.034917](#).
- [47] Zbigniew Drogosz, Wojciech Florkowski, Nikodem Witkowski, and Radosław Ryblewski.  $^3\text{H}$  and  $^3\text{He}$  nuclei production in a combined thermal and coalescence framework for heavy-ion collisions in the few-GeV energy regime\*. *Chin. Phys.*, 50(1):014104, 2026. [arXiv:2504.00283](#), [doi:10.1088/1674-1137/ae099a](#).
- [48] Ulrich W. Heinz. Concepts of heavy ion physics. In *2nd CERN-CLAF School of High Energy Physics*, pages 165–238, 7 2004. [arXiv:hep-ph/0407360](#).
- [49] J. D. Bjorken. Highly Relativistic Nucleus-Nucleus Collisions: The Central Rapidity Region. *Phys. Rev. D*, 27:140–151, 1983. [doi:10.1103/PhysRevD.27.140](#).
- [50] Derek Teaney. The Effects of viscosity on spectra, elliptic flow, and HBT radii. *Phys. Rev. C*, 68:034913, 2003. [arXiv:nucl-th/0301099](#), [doi:10.1103/PhysRevC.68.034913](#).
- [51] Amaresh Jaiswal and Volker Koch. A viscous blast-wave model for relativistic heavy-ion collisions. 8 2015. [arXiv:1508.05878](#).
- [52] Z. Yang and Rainer J. Fries. A Blast Wave Model With Viscous Corrections. *J. Phys. Conf. Ser.*, 832(1):012056, 2017. [arXiv:1612.05629](#), [doi:10.1088/1742-6596/832/1/012056](#).
- [53] Zhidong Yang and Rainer J. Fries. Shear stress tensor and specific shear viscosity of hot hadron gas in nuclear collisions. *Phys. Rev. C*, 105:014910, Jan 2022. URL: <https://link.aps.org/doi/10.1103/PhysRevC.105.014910>, [doi:10.1103/PhysRevC.105.014910](#).
- [54] Zhidong Yang and Rainer J. Fries. Parameterizing smooth viscous fluid dynamics with a viscous blast wave. *J. Phys. G*, 51(1):015102, 2024. [arXiv:2007.11777](#), [doi:10.1088/1361-6471/ad0914](#).
- [55] Zhidong Yang and Lie-Wen Chen. Bayesian inference of the specific shear and bulk viscosities of the quark-gluon plasma at crossover from  $\phi$  and  $\Omega$  observables. *Phys. Rev. C*, 107(6):064910, 2023. [arXiv:2207.13534](#), [doi:10.1103/PhysRevC.107.064910](#).
- [56] Zhidong Yang, Yifeng Sun, and Lie-Wen Chen. Baryon-density dependence of viscosities of the quark-gluon plasma at hadronization. *Phys. Rev. C*, 109(5):054907, 2024. [arXiv:2310.17444](#), [doi:10.1103/PhysRevC.109.054907](#).
- [57] Ralf Rapp and Jochen Wambach. Low mass dileptons at the CERN SPS: Evidence for chiral restoration? *Eur. Phys. J. A*, 6:415–420, 1999. [arXiv:hep-ph/9907502](#), [doi:10.1007/s100500050364](#).
- [58] Ralf Rapp and Edward V. Shuryak. Thermal dilepton radiation at intermediate masses at the CERN - SPS. *Phys. Lett. B*, 473:13–19, 2000. [arXiv:hep-ph/9909348](#), [doi:10.1016/S0370-2693\(99\)01367-2](#).
- [59] R. Rapp. Signatures of thermal dilepton radiation at RHIC. *Phys. Rev. C*, 63:054907, 2001. [arXiv:hep-ph/0010101](#), [doi:10.1103/PhysRevC.63.054907](#).
- [60] Simon Turbide, Ralf Rapp, and Charles Gale. Hadronic production of thermal photons. *Phys. Rev. C*, 69:014903, 2004. [arXiv:hep-ph/0308085](#), [doi:10.1103/PhysRevC.69.014903](#).
- [61] Hendrik van Hees, Vincenzo Greco, and Ralf Rapp. Heavy-quark probes of the quark-gluon plasma and interpretation of recent data taken at the BNL Relativistic Heavy Ion Collider. *Phys. Rev. C*, 73:034913, 2006. [arXiv:nucl-th/0508055](#), [doi:10.1103/PhysRevC.73.034913](#).
- [62] Hendrik van Hees and Ralf Rapp. Comprehensive interpretation of thermal dileptons at the SPS. *Phys. Rev. Lett.*, 97:102301, 2006. [arXiv:hep-ph/0603084](#), [doi:10.1103/PhysRevLett.97.102301](#).
- [63] Hendrik van Hees and Ralf Rapp. Dilepton Radiation at the CERN Super Proton Synchrotron. *Nucl. Phys. A*, 806:339–387, 2008. [arXiv:0711.3444](#), [doi:10.1016/j.nuclphysa.2008.03.009](#).
- [64] Hendrik van Hees, Charles Gale, and Ralf Rapp. Thermal Photons and Collective Flow at the Relativistic Heavy-Ion Collider. *Phys. Rev. C*, 84:054906, 2011. [arXiv:1108.2131](#), [doi:10.1103/PhysRevC.84.054906](#).
- [65] Pol Bernard Gossiaux, Sascha Vogel, Hendrik van Hees, Joerg Aichelin, Ralf Rapp, Min He, and Marcus Bluhm. The Influence of bulk evolution models on heavy-quark phenomenology. 2 2011. [arXiv:1102.1114](#).
- [66] Hendrik van Hees, Min He, and Ralf Rapp. Pseudocritical enhancement of thermal photons in relativistic heavy-ion collisions? *Nucl. Phys. A*, 933:256–271, 2015. [arXiv:1404.2846](#), [doi:10.1016/j.nuclphysa.2014.09.009](#).
- [67] Ralf Rapp and Hendrik van Hees. Thermal Dileptons as Fireball Thermometer and Chronometer. *Phys. Lett. B*, 753:586–590, 2016. [arXiv:1411.4612](#), [doi:10.1016/j.physletb.2015.12.065](#).
- [68] Fred Cooper and Graham Frye. Comment on the Single Particle Distribution in the Hydrodynamic and Statistical Thermodynamic Models of Multiparticle Production. *Phys. Rev. D*, 10:186, 1974. [doi:10.1103/PhysRevD.10.186](#).
- [69] L. Adamczyk et al. Beam-energy-dependent two-pion interferometry and the freeze-out eccentricity of pions measured in heavy ion collisions at the STAR detector. *Phys. Rev. C*, 92(1):014904, 2015. [arXiv:1403.4972](#), [doi:10.1103/PhysRevC.92.014904](#).
- [70] J. Cleymans and K. Redlich. Unified description of freezeout parameters in relativistic heavy ion collisions. *Phys. Rev. Lett.*, 81:5284–5286, 1998. [arXiv:nucl-th/9808030](#), [doi:10.1103/PhysRevLett.81.5284](#).
- [71] A. Andronic, P. Braun-Munzinger, and J. Stachel. Hadron production in central nucleus-nucleus collisions at chemical freeze-out. *Nucl. Phys. A*, 772:167–199, 2006. [arXiv:nucl-th/0511071](#), [doi:10.1016/j.nuclphysa.2006.03.012](#).
- [72] J. Cleymans and K. Redlich. Chemical and thermal freezeout parameters from 1-A/GeV to 200-A/GeV. *Phys. Rev. C*, 60:054908, 1999. [arXiv:nucl-th/9903063](#), [doi:10.1103/PhysRevC.60.054908](#).
- [73] Djamel Ouerdane. Rapidity dependence of charged particle yields for Au+Au at  $\sqrt{s_{NN}} = 200\text{-GeV}$ . *Nucl.*

- Phys. A*, 715:478–481, 2003. [arXiv:nucl-ex/0212001](#), [doi:10.1016/S0375-9474\(02\)01454-9](#).
- [74] S. V. Afanasiev et al. Energy dependence of pion and kaon production in central Pb + Pb collisions. *Phys. Rev. C*, 66:054902, 2002. [arXiv:nucl-ex/0205002](#), [doi:10.1103/PhysRevC.66.054902](#).
- [75] J. Adamczewski-Musch et al. Charged-pion production in Au + Au collisions at  $\sqrt{s_{NN}} = 2.4$  GeV: HADES Collaboration. *Eur. Phys. J. A*, 56(10):259, 2020. [arXiv:2005.08774](#), [doi:10.1140/epja/s10050-020-00237-2](#).
- [76] L. Adamczyk et al. Elliptic flow of identified hadrons in Au+Au collisions at  $\sqrt{s_{NN}} = 7.7$ -62.4 GeV. *Phys. Rev. C*, 88:014902, 2013. [arXiv:1301.2348](#), [doi:10.1103/PhysRevC.88.014902](#).